

## Practical dynamic reliability analysis with spatiotemporal features in geotechnical engineering

Yu Otake, Kyohei Shigeno, Yosuke Higo & Shogo Muramatsu

**To cite this article:** Yu Otake, Kyohei Shigeno, Yosuke Higo & Shogo Muramatsu (2022) Practical dynamic reliability analysis with spatiotemporal features in geotechnical engineering, Georisk: Assessment and Management of Risk for Engineered Systems and Geohazards, 16:4, 662-677, DOI: [10.1080/17499518.2021.1971250](https://doi.org/10.1080/17499518.2021.1971250)

**To link to this article:** <https://doi.org/10.1080/17499518.2021.1971250>



© 2022 The Author(s). Published by Informa UK Limited, trading as Taylor & Francis Group



Published online: 29 Aug 2021.



Submit your article to this journal [↗](#)



Article views: 2656



View related articles [↗](#)





View Crossmark data [↗](#)



Citing articles: 10 View citing articles [↗](#)

# Practical dynamic reliability analysis with spatiotemporal features in geotechnical engineering

Yu Otake <sup>a</sup>, Kyohei Shigeno<sup>b</sup>, Yosuke Higo<sup>c</sup> and Shogo Muramatsu <sup>d</sup>

<sup>a</sup>Department of Civil and Environmental Engineering, Graduate School of Engineering, Tohoku University, Sendai, Miyagi, Japan; <sup>b</sup>Graduate School of Science and Technology, Niigata University, Niigata City, Niigata, Japan; <sup>c</sup>Department of Urban Management, Kyoto University, Japan; <sup>d</sup>Department of Electrical and Electronics Engineering, Niigata University, Niigata-city, Niigata, Japan

## ABSTRACT

In recent years, improvements to the design of earth structures to ensure soil robustness against accidental disaster load conditions has gained considerable importance. In this paper, we propose a practical reliability analysis scheme that can enable the development of a robust design based on dimensionality reduction; this scheme employs input parameters, and it uses numerical analysis results as multidimensional information while preserving the spatiotemporal information to the maximum extent. Further, the proposed design scheme has practical design functions similar to those of conventional reliability analysis methods, such as the first-order second-moment method and first-order reliability method. Finally, the effectiveness of the proposed design scheme and its significant contribution to the practical design of earth structures are demonstrated via a time series seismic deformation analysis of simple embankments on liquefiable sand ground.

## ARTICLE HISTORY

Received 28 December 2020  
Accepted 5 July 2021



## KEYWORDS

Reliability analysis; mode decomposition; seismic deformation; liquefaction

## 1. Introduction

Performance- and reliability-based designs have become standards for global structural design (American Association of State Highway and Transportation Officials, 2004; ISO2394, 1998; CEN, EN 1997-1 Eurocode 7, 2004). Recently, Japan has started introducing principle design codes such as the Technical Standards and Commentaries for Port and Harbor Facilities in Japan (Japan Port and Harbor Association (JPHA), 2007, 2018), Design Standards for Railway Structures and Commentary (Railway Technical Research Institute (RTRI), 2013), and Specifications for Highway Bridges and Commentary (Japan Road Association (JRA), 2017). In recent years, reliability assessment methods with reliability updates based on additional observation information and risk-informed design methods have become more practical (American Association of State Highway and Transportation Officials, 2003; Jongejan et al., 2013; Schweckendiek, 2014; Schultz van Haegen, 2016; ISO2394, 2015). Further, the concepts of robustness (ISO2394, 2015), resilience (Bruneau et al., 2003), and anticatastrophe (Honda et al., 2016) have received considerable attention as suitable methods for controlling accidental loading.

The aim of this study was to develop a practical framework of soil structures to achieve robustness and resilience against accidental loading. We propose to introduce a failure mode guided design, as shown in the conventional seismic structural design (e.g. the horizontal load-bearing capacity method during earthquakes) (Japan Road Association (JRA), 1996), by limiting plasticisation – an approach commonly practiced in structural engineering – in soil structures. To actively control the failure modes in earth structures, it is necessary to check whether the failure modes remain acceptable while increasing the magnitude of the external force. In this case, it is essential to introduce numerical analysis for direct evaluation of the failure mode to assess the performance of the structure. Moreover, it is necessary to develop robust control techniques that incorporate the effects of uncertainty in the external forces and spatial distribution of soil profiles. In this paper, as a first step, we propose a framework for efficient reliability analysis while preserving the spatiotemporal information contained in the numerical analysis. However, the evaluation of the influence of other important factors (uncertainty in external forces, spatial distribution of soil profiles, and model error in

**CONTACT** Yu Otake  [yu.otake.b6@tohoku.ac.jp](mailto:yu.otake.b6@tohoku.ac.jp)  Department of Civil and Environmental Engineering, Graduate School of Engineering, Tohoku University, 6-6-06 Aramaki Aoba, Aoba, Sendai, Miyagi 980-8579, Japan

© 2021 The Author(s). Published by Informa UK Limited, trading as Taylor & Francis Group

This is an Open Access article distributed under the terms of the Creative Commons Attribution-NonCommercial-NoDerivatives License (<http://creativecommons.org/licenses/by-nc-nd/4.0/>), which permits non-commercial re-use, distribution, and reproduction in any medium, provided the original work is properly cited, and is not altered, transformed, or built upon in any way.

numerical analysis) is a future endeavour and beyond the scope of discussion in this paper.

For developing a practical framework, in this study, we evaluated the seismic settlement process of a simple embankment on a liquefied ground. We attempted to develop a practical method for quantifying the uncertainties, in the input parameter setting, and propagating them into the reliability of the spatiotemporal behaviour of embankments by combining the effective stress dynamic finite element method (LIQCA) (Liquefaction analysis method LIQCA Development group, 2007; Oka et al., 1994, 1999; Danjo et al., 2018; Hirota et al., 2017) and the reliability analysis. Such sophisticated numerical analysis requires physical input parameters that can be measured, and fitting parameters that are difficult to set objectively. By collecting numerous examples of expert input parameter settings for the LIQCA analysis, we considered modelling the input parameters with a multidimensional probability distribution (prior distribution) and quantifying the uncertainties in the parameters arising from the conditional probability in some physical parameters observed at the site (posterior distribution).

Next, we analysed the uncertainty propagation, while setting the input parameters, into the numerical results. Further, the input parameters, time series of the nodal displacements, and elemental stresses obtained from the numerical analysis are considered as multidimensional information. Mode decomposition (PCA: Principle component analysis (Pearson, 1901; Liang et al., 2002; Jolliffe, 2002), POD: Proper orthogonal decomposition (Chatterjee, 2000; Sirovich, 1987; Berkooz, Holmes, and Lumley, 2003)) and dimensionality reduction are performed for both of them (Otake et al., 2019a). Reliability analysis (i.e. propagation analysis of input parameter uncertainty) is performed using the alternative calculation model (reduced order model; ROM) constructed via simple linear regression analysis on the feature space (eigenspace). This study provides a simplified reliability analysis framework with spatiotemporal features that can evaluate failure modes and which follows the concept of traditional simplified reliability analysis FOSM: first-order second-moment method (Cornell, 1969) and FORM: first-order reliability method (Hasofer and Lind, 1974) based on a linear approximation at the mean values and design point.

## 2. Simplified reliability analysis framework with ROM and issues

Figure 1 shows the proposed simplified reliability analysis framework. Before providing the detailed

formulation, we provide an outline of this framework and clarify its issues in this section. Further, the expressions and symbols shown in the figure are described later. Here, we present only an overview.

The proposed analysis framework is largely divided into two parts: initial data processing and analysis.

### 2.0.1. Initial data processing

First, the input parameter set for the constitutive laws used in numerical analysis are collected. We strive to gather as many input parameter sets from as diverse a range of conditions as possible; however, we restrict the parameter sets to those provided by experts with reliability. The input parameter set is modelled as a multivariate normal distribution; the eigenvalue and mode (i.e. vector) are calculated by the principal component analysis (PCA) of the covariance matrix. Considering reconstruction using only the main eigenmode, the information can be reduced to lower dimensional data. Another method involves using sparse modelling (Tibshirani, 1996) and similar methods to reduce the number of dimensions objectively; however, we prioritise an engineering-based interpretation and recommend that the analyst make decisions while observing and considering the engineering features of the input parameters that appear in the eigenmodes in this study.

### 2.0.2. Analysis part

The multivariate normal distribution, created during the initial data processing, is used as a prior distribution for performing Bayesian analysis based on the partial information and constraint conditions obtained on-site to produce a posterior distribution (i.e. multivariate normal distribution) of the input parameters that reflect the on-site features.

Design experiments (DEs) are performed using this posterior distribution, and the numerical analysis time-series data (i.e. collection of snapshots from multiple cases based on the time point) of various cases (i.e. numerical experiments) are acquired. The eigenvalues and eigenmodes are calculated by using the POD of the numerical analysis time series data covariance matrix. Although PCA and POD are consistent in theory, we intentionally distinguish between them in this paper; PCA is used for an input parameter set, and POD is used for the numerical analysis of the time-series data.

Similar to the engineering features of the input parameters, those that appear in the main modes and component coefficients are observed and considered. Further, we design an ROM that considers the spatiotemporal information by conducting a simple linear

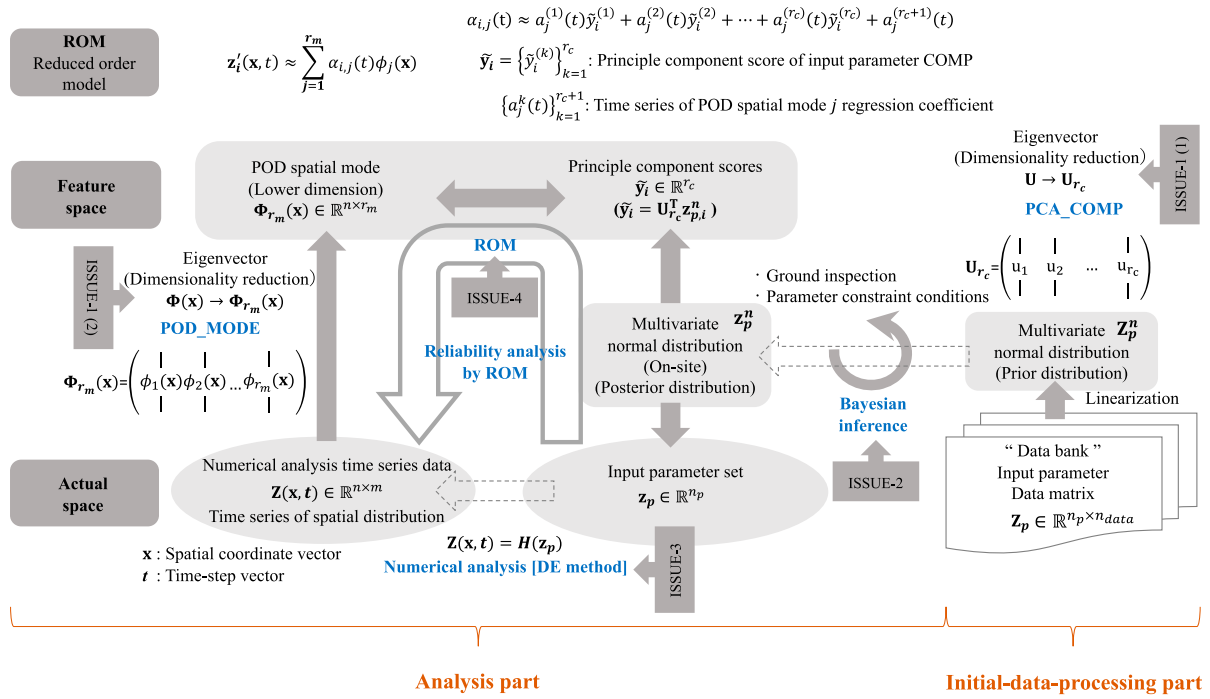


Figure 1. Proposed alternative model construction framework.

regression analysis (i.e. linear combination) of the reduced number of dimensions of the input parameters and the those of the spatial distribution of the analysis result (i.e. response value). The uncertainty propagation can be analysed using the expected value characteristics by expressing them using a linear combination.

We can perform a reliability analysis (uncertainty propagation analysis of the input parameter setting uncertainty) using the expected value characteristics by dimensionally reducing the input parameter set and analysis results, and by utilising their linear combination. The five primary issues shown in Figure 1 are listed below.

- **ISSUE-1: Mode decomposition (PCA and POD):** Calculation methods, based on the mode decomposition (POD) of the numerical analysis time series data, are presented as examples. We examine the basic idea of mode decomposition by using singular value decomposition (SVD), and by determining an approach to construct a data matrix (containing the results of the numerical analysis) for the SVD.
- **ISSUE-2: Bayesian inference-based input parameter estimation:** Previous samples of input parameter sets in various conditions, set up by numerical analysis experts, are collected and a prior distribution of input parameters is created (as multivariable normal distribution). Next, we present a process for

obtaining a posterior distribution (uncertainty in input parameter settings) that is suitable for the target site from the partial information that can be observed at that site.

- **ISSUE-3: DEs for deriving ROM:** The idea is to create a simple ROM with a linear approximation of the relationship between the input parameters and numerical analysis results, near the average value of the input parameters. A simple DE based on this concept is designed.
- **ISSUE-4: ROM construction:** We present an efficient regression analysis method to derive an equation (ROM) for estimating the time evolution of the component coefficient of the POD space modes.
- **ISSUE-5: Uncertainty propagation and sensitivity analyses:** Input parameter uncertainty can be analytically converted into the uncertainty of numerical analyses using the expected value characteristics. We demonstrate that a sensitivity analysis (equivalent to the sensitivity coefficient in the FORM method) of the entire computational spatial domain on FEM can be computed easily.

### 2.0.3. Basic analysis method

Although the proposed analysis scheme does not specify the numerical analysis methods, we conducted a concrete analysis procedure based on a case study using an effective stress dynamic analysis (LIQCA)

(Liquefaction analysis method LIQCA Development group, 2007). Governing equations of LIQCA are the equations of motion for the soil–water mixture and the continuity equation for pore water, based on the two-phase mixture theory (e.g. Zienkiewicz and Shiomi, 1984). The equations of motion and the continuity equation are discretised using the finite element and finite difference methods, respectively.

The cyclic elastic–plastic model of sand, developed by Oka et al. (1994, 1999), Danjo et al. (2018) and Hirota et al. (2017), was used as the constitutive model for describing the relationship between the effective stress and strain of liquefiable soil.

As listed in Table 1, this constitutive model requires 13 parameters, comprising 7 physical parameters and 6 fitting parameters. The seven physical parameters are determined via soil laboratory tests and field observations, whereas the six fitting parameters are determined via comparisons of the liquefaction strength curves obtained from cyclic triaxial tests and element using the constitutive model to obtain good agreement with the test results. For the determination of the fitting parameters, a high level of knowledge and experience with the constitutive model is required.

One of the most important features of this analysis scheme is imparting objectivity to the input parameter design process with prior data collection and Bayesian inference as well as reflecting the uncertainty in the analysis result (i.e. response value). Table 1 summarises the analysis parameter examples designed for 19 examples. We conducted each soil test (e.g. standard physical tests, dynamic deformation tests, and liquefaction strength tests) in this study and consolidated the input parameter sets designated by experts based on these soil tests. The number (i.e. examples) of input parameter sets is small and further data collection is necessary; however, a diverse set of examples, such as natural sedimentary ground and artificially reclaimed land, are included in addition to the standard sand for the experiments (e.g. Toyoura sand (DS-1)). We determined that the feature extraction of the parameter set was possible.

### 3. Research methods

#### 3.1. ISSUE-1: mode decomposition (PCA and POD)

We discuss examples of the mode decomposition (POD) of the time series data of the numerical analysis results. For the mode decomposition of the input parameters (PCA), only the data matrix  $\mathbf{Z}$  (Equation (2)) shown below needs to be substituted by the data matrix  $\mathbf{Z}_p$  (Equation (6)) that stores the various collected input

**Table 1.** List of collected input parameter sets (initial data).

	Physical parameter							Fitting parameter							Reference
	$e_0$	$\lambda$	$\kappa$	OCR*	$G_0/\sigma'_m$	$M_f^*$	$M_m^*$	$B_0^*$	$B_1^*$	$\gamma_r^{p*}$	$\gamma_r^{f*}$	$D_0^*$	$n$		
DS-1	0.754	0.0091	0.0005	1.0	2023	0.990	0.707	4089	54	0.002	0.012	0.6	5.1	Reference (Liquefaction analysis method LIQCA Development group, 2007), Toyoura sand ( $D_r=60\%$ ) Reference (Liquefaction analysis method LIQCA Development group, 2007), No.7 silica sand ( $D_r=90\%$ ) Reference (Liquefaction analysis method LIQCA Development group, 2007), Rokko island fill material Reference (Liquefaction analysis method LIQCA Development group, 2007), Albany sand ( $D_r=70\%$ ) Reference (Liquefaction analysis method LIQCA Development group, 2007), Toyoura sand ( $D_r=60\%$ ) Reference (Liquefaction analysis method LIQCA Development group, 2007), Embankment Reference (Liquefaction analysis method LIQCA Development group, 2007), Landfill sand layer Reference (Liquefaction analysis method LIQCA Development group, 2007), Edosaki sand ( $D_r=50\%$ ) Reference (Liquefaction analysis method LIQCA Development group, 2007), Port island fill material Reference (Liquefaction analysis method LIQCA Development group, 2007), Landfill soil Reference (Danjo et al., 2018), Miyakojima upper sand layer Reference (Danjo et al., 2018), Miyakojima lower sand layer Reference (Danjo et al., 2018), Nishijima upper sand layer Reference (Danjo et al., 2018), Nishijima lower sand layer Reference (Danjo et al., 2018), Kobayashi lower sand layer Reference (Hirota et al., 2017), No.7 silica sand Reference (Otake and Honjo, 2012), Upper sand layer Reference (Otake and Honjo, 2012), Upper sand layer Reference (Otake and Honjo, 2012), Upper sand layer	
DS-2	0.673	0.0250	0.0025	1.0	908	1.511	0.909	1500	20	0.015	0.100	1.0	9.0		
DS-3	0.500	0.0100	0.0100	1.0	1894	1.340	0.909	3900	98	0.002	0.005	1.0	8.0		
DS-4	0.558	0.0009	0.0005	1.2	1250	1.308	0.800	3000	100	0.020	0.020	0.8	7.0		
DS-5	0.752	0.0250	0.0025	1.0	1317	0.960	0.710	6000	60	0.002	0.020	1.0	2.0		
DS-6	0.856	0.0180	0.0055	1.0	873	1.122	0.909	2200	30	0.005	0.010	5.0	1.5		
DS-7	0.420	0.0100	0.0010	1.0	1517	1.200	0.910	3500	70	0.002	0.010	1.0	4.0		
DS-8	0.856	0.0180	0.0055	1.0	873	1.122	0.909	2200	30	0.005	0.010	5.0	1.5		
DS-9	0.420	0.0100	0.0100	1.0	730	1.340	0.909	1500	150	0.005	0.005	1.0	4.0		
DS-10	0.800	0.0250	0.0003	1.0	761	1.229	0.909	2000	40	0.005	0.003	1.0	4.0		
DS-11	0.900	0.0087	0.0055	1.0	430	1.254	0.843	3000	10	0.005	0.100	1.0	2.0		
DS-12	1.230	0.0087	0.0055	1.0	178	1.200	0.980	2000	20	0.008	0.100	1.0	2.4		
DS-13	0.830	0.0087	0.0055	1.0	355	1.306	0.907	1000	10	0.010	0.009	1.0	2.0		
DS-14	0.940	0.0087	0.0055	1.0	266	1.270	0.852	1500	15	0.005	0.100	1.0	3.0		
DS-15	0.880	0.0180	0.0055	1.0	374	1.306	0.755	2000	30	0.005	0.100	1.0	7.0		
DS-16	0.850	0.0277	0.0092	1.0	989	1.015	0.838	2000	100	0.005	0.001	3.0	2.0		
DS-17	0.670	0.0033	0.0008	1.1	790	1.157	0.908	6800	72	0.007	0.058	0.7	7.0		
DS-18	0.760	0.0057	0.0014	1.1	630	1.122	0.908	6200	80	0.007	0.030	2.0	5.0		
DS-19	1.000	0.0046	0.0013	1.1	600	1.050	0.908	5400	80	0.006	0.024	2.0	5.0		



parameter sets. Thus, we exclude the explanation of this substitution here.

We set the state vector  $\mathbf{z}(\mathbf{x}, t) \in \mathbb{R}^n$  for a finite element model (FEM) result at a given time  $t$  (i.e. a snapshot). The three partial state vectors of the horizontal displacement  $\mathbf{z}_{d_x}(\mathbf{x}_n, t)$  and vertical displacement  $\mathbf{z}_{d_y}(\mathbf{x}_n, t)$  of each node, and the excess pore water pressure ratio  $\mathbf{z}_{epwp}(\mathbf{x}_e, t)$  of each element are used to create the vector.

$$\mathbf{z}(\mathbf{x}, t) = \begin{bmatrix} \mathbf{z}_{d_x}^T(\mathbf{x}_n, t) & \mathbf{z}_{d_y}^T(\mathbf{x}_n, t) & \mathbf{z}_{epwp}^T(\mathbf{x}_e, t) \end{bmatrix}^T \quad (1)$$

Here,  $\mathbf{x}_n$ ,  $\mathbf{x}_e$ , and  $\mathbf{x}$  denote the spatial coordinate vector of the FEM model nodes (i.e. the coordinates of all contact points), the spatial coordinate vector of the FEM elements (i.e. the coordinates or integration points of all elements), and the spatial coordinate of the node and element that correspond to the partial state vector, respectively.

In these cases,  $n$  denotes the total dimension number of the partial state vector; its value is equal to node number  $n_n \times 2 +$  element number  $n_e$ . The analysis results are from time  $t_1$  to  $t_m$ , and when output at an interval  $\Delta t$ , the state vector  $\{\mathbf{z}(\mathbf{x}, t_1), \mathbf{z}(\mathbf{x}, t_2), \dots, \mathbf{z}(\mathbf{x}, t_m)\}$  for each time point is entered into data matrix  $\mathbf{Z} \in \mathbb{R}^{n \times m}$  in the order of the time series as shown below.

$$\mathbf{Z} = \begin{bmatrix} \mathbf{z}(\mathbf{x}, t_1) & \mathbf{z}(\mathbf{x}, t_2) & \dots & \mathbf{z}(\mathbf{x}, t_m) \end{bmatrix} \quad (2)$$

The time-averaged vector  $\bar{\mathbf{z}} \in \mathbb{R}^n$  is expressed as:

$$\bar{\mathbf{z}} = \frac{1}{m} \sum_{k=1}^m \mathbf{z}(\mathbf{x}, t_k) \quad (3)$$

where  $\bar{\mathbf{z}}$  is subtracted from the state vector of each time frame, and a matrix of these values is defined as  $\mathbf{Z}' \in \mathbb{R}^{n \times m}$ . We efficiently calculated the spatial mode based on the SVD of  $\mathbf{Z}'$  as

$$\mathbf{Z}' = \mathbf{U}\mathbf{D}\mathbf{V}^T \simeq \mathbf{U}_r\mathbf{D}_r\mathbf{V}_r^T \quad (4)$$

where  $\mathbf{U} \in \mathbb{R}^{n \times n}$ ,  $\mathbf{V} \in \mathbb{R}^{n \times m}$ , and  $\mathbf{D} \in \mathbb{R}^{m \times m}$  denote the matrices containing the spatial mode vectors  $\mathbf{u}_j$ ; the component coefficient vectors  $\mathbf{v}_j$ , expressed as the time series of each contributing POD spatial mode  $\mathbf{v}_j$ ; and a singular value matrix containing the values  $d_j$  corresponding to  $\mathbf{u}_j$ , arranged diagonally; respectively.

At this point, modes that can be interpreted from an engineering perspective are selected in the order of ascending eigenvalues. When the number of modes necessary for expressing the original data (primary mode number) is set as  $r$ , these modes are approximated using the information contraction shown above. Here,  $\mathbf{U}_r \in \mathbb{R}^{n \times r}$  is a reduced-dimensionality matrix created

by ordering the POD spatial modes numbering  $r$  in total in the ascending order of eigenvalues.

$\mathbf{V}_r \in \mathbb{R}^{m \times r}$  and  $\mathbf{D}_r \in \mathbb{R}^{r \times r}$  are the matrices corresponding to a reduced-dimensionality matrix  $\mathbf{U}_r$ . The contribution  $C_{ont}(j)$  of the POD spatial mode  $j$  is defined as:

$$C_{ont}(j) = \frac{d_j^2}{\sum_{j=1}^n d_j^2} = \frac{\lambda_j}{\sum_{j=1}^n \lambda_j} \quad (5)$$

where  $C_{ont}(j)$  corresponds to the ratio of the eigenvalue  $\lambda_j$  to the covariance matrix  $\mathbf{Z}'\mathbf{Z}'^T$ .

### 3.2. ISSUE-2: Bayesian inference-based input parameter estimation

The input parameter sets, accumulated during the initial data processing, are consolidated as a data matrix  $\mathbf{Z}_p \in \mathbb{R}^{n_p \times n_{data}}$ , which is similar to those of the numerical analysis time series data (Equation (2)).

$$\mathbf{Z}_p = \begin{bmatrix} \mathbf{z}_{p,1} & \mathbf{z}_{p,2} & \dots & \mathbf{z}_{p,n_{data}} \end{bmatrix} \quad (6)$$

where  $n_p$ ,  $n_{data}$ , and  $\mathbf{z}_{p,i} \in \mathbb{R}^{n_p}$  denote the number of input parameters for the numerical analysis, number of collected parameter sets, and a given input parameter set vector. Further,  $\mathbf{z}_p(h)$  denotes the  $h^{th}$  row vector (i.e.  $h^{th}$  parameter) of  $\mathbf{z}_p$ ; the probability distribution of  $\mathbf{z}_p(h)$  is defined as  $F(\mathbf{z}_p(h))$ .

We recommend that probability distribution and the distribution parameter should be set for each parameter; however, in this study, all parameters are nonnegative, and the distribution tails become longer as the parameter values increase. Therefore, we utilise a logarithmic normal distribution. However, the model for the probability density of the input parameters is based on extremely simple assumptions because a sufficient data set is not available currently.

The distribution parameters were transformed into standard normal distributions using the transformation shown below, which is similar to that reported in Rezaeian and Der Kiureghian (2010), Ching and Phoon (2019), Ching and Phoon (2020) and Otake, Watanabe, and Mizutani (2021). The distributions were then simulated as a multivariate standard normal distribution.

$$\mathbf{z}_p^n(h) = \Phi_{norm}^{-1}[F(\mathbf{z}_p(h))](h = 1, 2, \dots, n_p) \quad (7)$$

where  $\Phi_{norm}^{-1}[\cdot]$  refers to the inverse function of the standard normal distribution. The distribution parameters for the probability distribution  $F(\mathbf{z}_p(h))$ ,  $h = 1, \dots, n_p$  that correspond to each parameter are listed in Table 2. As the probability distribution of each parameter is different here, it is difficult to model simply the correlation structure. Here, the distribution is modelled as a

**Table 2.** Distribution parameters of the input parameters (modelled as logarithmic normal distribution).

	Distribution parameters	
	$\mu_{\ln x}$	$\sigma_{\ln x}$
$e_0$	-0.29	0.28
$\lambda$	-4.66	0.80
$\kappa$	-6.26	0.97
OCR*	0.034	0.06
$G_0/\sigma'_m$	6.60	0.63
$M_f^*$	0.18	0.12
$M_m^*$	-0.15	0.09
$B_0^*$	7.96	0.55
$B_1^*$	3.76	0.80
$\gamma_r^{P*}$	5.13	0.80
$\gamma_r^{F*}$	3.93	1.20
$D_0^*$	0.16	0.57
$n$	1.32	0.56

multivariate standard normal distribution after individually transforming the distribution to a standard normal distribution. In other words, the correlation among the parameters is maintained and updated to a more manageable index as a covariance matrix, as shown below. We interpret the correlation coefficient as a meaningful indicator in the case of linear relationships. The correlation coefficients between arbitrary indicator distributions before transforming to standard normal distribution are considered as apparent values. We redefine the covariance matrix after transforming it to the standard normal distribution for each indicator – the correlation structure updates – based on some corrections depending on the distribution transformation.

Based on the assumption that each parameter is a random variable, the random variable vector  $\mathbf{x}$  is defined as

$$\mathbf{x} = \left( \mathbf{z}_p^n(1), \mathbf{z}_p^n(2), \dots, \mathbf{z}_p^n(n_p) \right)^T \quad (8)$$

The arrangement of the average value of each parameter  $\boldsymbol{\mu}$  is expressed as:

$$\boldsymbol{\mu} = \left( \bar{\mathbf{z}}_p^n(1), \bar{\mathbf{z}}_p^n(2), \dots, \bar{\mathbf{z}}_p^n(n_p) \right)^T \quad (9)$$

Then, after  $\bar{\mathbf{z}}_p^n(h)$  is subtracted from each parameter vector, the arranged matrix is defined as  $\mathbf{Z}_p^{n'} \in \mathbb{R}^{n_p \times n_{data}}$ . The covariance matrix  $\boldsymbol{\Sigma} \in \mathbb{R}^{n_p \times n_p}$  is defined as

$$\boldsymbol{\Sigma} = \mathbf{Z}_p^{n'} \mathbf{Z}_p^{n'T} \quad (10)$$

where  $\boldsymbol{\mu}$  and  $\boldsymbol{\Sigma}$  denote the design uncertainties of the input parameters when there is no additional on-site information. Further, they are the distribution parameters of the prior distributions in the Bayesian inference. In cases where a portion of the parameter random variable vectors are observed on-site, the following procedure can be used to obtain Bayesian inference and posterior distribution.

Here,  $\mathbf{x}$  is divided into two partial vectors:  $\mathbf{x}_1$  of the known random variable observed at the location (i.e.  $e_0$ ,  $G_0/\sigma'_m$  and  $\phi'$ ) and  $\mathbf{x}_2$  of the unknown random variable.

When the random variables follow a normal distribution,  $\mathbf{x}_1$  follows a normal distribution even when  $\mathbf{x}_2$  is given; thus, the posterior distribution parameters can be calculated analytically (Hoshiya and Yoshida, 1996; Yoshida et al., 2018).

### 3.3. ISSUE-3: DEs for deriving ROM

To create the ROM model, the time series data  $\mathbf{Z}$  should be efficiently accumulated by implementing planned numerical analysis. We propose a DE based on the projection of  $\tilde{\mathbf{Y}}_p = \mathbf{U}_{z_p, r_c}^T \mathbf{Z}_p^{n'}$  (i.e. the principal component score) into the eigenspace of  $\mathbf{Z}_p^{n'}$  if the dimensionality-reduced parameter COMP matrix is set as  $\mathbf{U}_{z_p, r_c}$ .  $\tilde{\mathbf{Y}}_p = \{\tilde{y}_i^{(1)}, \tilde{y}_i^{(2)} \dots \tilde{y}_i^{(r_c)}\}$  is a vector where the principal component scores are arranged in the ascending order of eigenvalues.

In the following application example, the case with  $r_c = 3$  is described. We explain the concrete computation procedure in the context of this example below. Table 3 lists the input parameter set for five cases around the mean for the designed experiment. The three columns on the left side of the table represent the principal component scores  $\tilde{\mathbf{Y}}_p^{(DE)}$ , and the input parameter set  $\mathbf{Z}_p^{n'(DE)}$  corresponding to the principal component scores are shown on the right side. Here, five cases are shown, including four cases based on the ( $L^4(2^3)$ ) design of the experiment, as well as the case where all principal component scores are zero (i.e. mean values case). As the principal components are not correlated with each other, the design of experiment can be set to a very simple ( $L^4(2^3)$ ), when the main objective is to obtain the gradient of the focus point

**Table 3.** Data processing (portion of implemented DE methods).

	$\tilde{y}_i^{(1)}$	$\tilde{y}_i^{(2)}$	$\tilde{y}_i^{(3)}$	$e_0$	$\lambda$	$\kappa$	OCR*	$G_0/\sigma'_m$	$M_f^*$	$M_m^*$	$B_0^*$	$B_1^*$	$\gamma_r^{P*}$	$\gamma_r^{F*}$	$D_0^*$	$n$
DE-1	0	0	0	0.773	0.0150	0.0030	1.0	882	1.200	0.878	2853	42	0.006	0.019	1.2	3.7
DE-2	+1	+1	+1	0.697	0.0062	0.0007	1.1	1023	1.236	0.845	4094	71	0.009	0.039	0.6	8.3
DE-3	+1	-1	-1	0.577	0.0191	0.0008	1.0	1549	1.099	0.855	4076	102	0.003	0.004	1.4	3.4
DE-4	-1	+1	-1	0.747	0.0204	0.0048	1.0	503	1.409	0.928	1226	21	0.006	0.026	1.3	3.6
DE-5	-1	-1	+1	0.476	0.0150	0.0005	1.0	1311	1.343	0.884	2513	83	0.005	0.009	0.8	7.3

(i.e. the mean values in this case). In this table, +1 means the principal component scores +1  $\sigma$  from the mean, and -1 implies the principal component scores -1  $\sigma$  from the mean values. The input parameter set  $\mathbf{Z}_p^{n(DE)}$  after transformation to the standard normal distribution can be calculated by  $(\mathbf{U}_{z_p, r_c}^T)^{-1} \tilde{\mathbf{Y}}_p^{(DE)}$ , and can be obtained by transforming to the actual distribution using Equation (7).

Here, we designed a minimal number of experiments by assuming a linear approximation of the relationship between the input parameters and numerical analysis results, around the mean value of the input parameters. Ideally, the ROM should be designed in two stages. It would be desirable to create an ROM around the mean, identify the design points using the ROM, and then perform a linear approximation around the design point. Due to technical considerations, we consider the average value to be the design point and show the process of planning the DEs and constructing the ROM around it.

### 3.4. ISSUE-4: ROM construction

We define  $\mathbf{Z}_i \in \mathbb{R}^{n \times m}$  as a time series data matrix, calculated according to a given numerical analysis (DE-*i* in Table 3). Further, the number of lower-dimension POD spatial modes used in the ROM model, is defined as  $r_m$ , and the POD spatial mode  $U_r$ , obtained from DE-1 (average value case), is defined as  $\tilde{\Phi} \in \mathbb{R}^{n \times r_m}$ .

$$\tilde{\Phi} = [\phi_1(\mathbf{x}) \quad \phi_2(\mathbf{x}) \quad \cdots \quad \phi_{r_m}(\mathbf{x})] \quad (11)$$

The state vector  $\mathbf{z}'_i(\mathbf{x}, t)$ , at time  $t$ , is given by

$$\begin{aligned} \mathbf{z}'_i(\mathbf{x}, t) &\simeq a_{i,1}(t)\phi_1(\mathbf{x}) + a_{i,2}(t)\phi_2(\mathbf{x}) + \cdots \\ &\quad + a_{i,r_m}(t)\phi_{r_m}(\mathbf{x}) \\ &= \sum_{j=1}^{r_m} a_{i,j}(t)\phi_j(\mathbf{x}) \end{aligned} \quad (12)$$

where  $a_{i,j}(t)$  denotes the temporal component coefficient corresponding to the eigenvector  $\phi_j(\mathbf{x})$ . This temporal component coefficient  $a_{i,j}(t)$  is associated with the primary component score  $\tilde{\mathbf{Y}}_p = (\tilde{y}_i^{(1)}, \tilde{y}_i^{(2)} \dots \tilde{y}_i^{(r_c)})^T$ .

$$\begin{aligned} a_{i,j}(t) &= a_j^{(1)}(t)\tilde{y}_i^{(1)} + a_j^{(2)}(t)\tilde{y}_i^{(2)} + \cdots + a_j^{(r_c)}(t)\tilde{y}_i^{(r_c)} \\ &\quad + a_j^{(r_c+1)}(t) \end{aligned} \quad (13)$$

Substituting Equation (13) into Equation (12) yields

$$\begin{aligned} \mathbf{z}'_i(\mathbf{x}, t) &\simeq \sum_{j=1}^{r_m} \{a_j^{(1)}(t)\tilde{y}_i^{(1)} + a_j^{(2)}(t)\tilde{y}_i^{(2)} + \cdots \\ &\quad + a_j^{(r_c)}(t)\tilde{y}_i^{(r_c)} + a_j^{(r_c+1)}(t)\}\phi_j(\mathbf{x}) \end{aligned} \quad (14)$$

Here, we create a partial matrix  $\phi_{ij}(\mathbf{x}) \in \mathbb{R}^{n \times (r_c+1)}$  to determine the regression coefficient efficiently and construct  $\Phi_i \in \mathbb{R}^{n \times (r_c+1) \times r_m}$ . Moreover,  $r_c$  is the number of lower dimension PCA modes corresponding to the input parameter set.

$$\phi_{ij}(\mathbf{x}) = [\tilde{y}_{i,1}\phi_j(\mathbf{x}) \quad \tilde{y}_{i,2}\phi_j(\mathbf{x}) \quad \cdots \quad \tilde{y}_{i,r_c}\phi_j(\mathbf{x}) \quad \phi_j(\mathbf{x})] \quad (15)$$

$$\Phi_i = [\phi_{i,1}(\mathbf{x}) \quad \phi_{i,2}(\mathbf{x}) \quad \cdots \quad \phi_{i,r_m}(\mathbf{x})] \quad (16)$$

A regression coefficient time series vector, corresponding to the input parameter COMP  $l$ , is defined as  $\mathbf{a}_j^{(l)} \in \mathbb{R}^m$  to create a corresponding matrix of unknown values (i.e. regression coefficients).

$$\mathbf{a}_j^{(l)} = (a_j^{(l)}(t_1), a_j^{(l)}(t_2), \dots, a_j^{(l)}(t_m))^T \quad (17)$$

We construct a regression coefficient time series matrix  $\mathbf{A}_j^{mode} \in \mathbb{R}^{(r_c+1) \times m}$  that corresponds to a POD spatial mode  $j$  by vertically aligning Equation (17).

$$\mathbf{A}_j^{mode} = [\mathbf{a}_j^{(1)} \quad \mathbf{a}_j^{(2)} \quad \cdots \quad \mathbf{a}_j^{(r_c)} \quad \mathbf{a}_j^{(r_c+1)}]^T \quad (18)$$

Next, we create a matrix where the time series matrices of all regression coefficients are aligned by vertically aligning the regression coefficient time series matrix  $\mathbf{A}_j^{mode}$  for all POD spatial modes.

$$\mathbf{A} = [\mathbf{A}_1^{mode^T} \quad \mathbf{A}_2^{mode^T} \quad \cdots \quad \mathbf{A}_{r_m}^{mode^T}]^T \quad (19)$$

The observed equation, corresponding to the implemented DE-*i* of the FEM from Equation (15) to (19), is given as

$$\mathbf{Z}'_i = \Phi_i \mathbf{A} \quad (20)$$

Equation (21) can be obtained by vertically aligning Equation (20) with the number of FEM implementations.

$$\mathbf{Z}'_{De} = \Phi_{De} \mathbf{A} \quad (21)$$

If the total number of FEM implementations based on DE is set as  $n_{cal}$ , then  $\Phi_{De} \in \mathbb{R}^{(n \times n_{cal}) \times \{(r_c+1) \times r_m\}}$  and



$\mathbf{Z}'_{De} \in \mathbb{R}^{(n \times n_{cal}) \times m}$  become matrices

$$\mathbf{Z}'_{De} = \begin{bmatrix} \mathbf{Z}'_1{}^T & \mathbf{Z}'_2{}^T & \cdots & \mathbf{Z}'_{n_{cal}}{}^T \end{bmatrix}^T \quad (22)$$

$$\Phi_{De} = \begin{bmatrix} \Phi_1^T & \Phi_2^T & \cdots & \Phi_{n_{cal}}^T \end{bmatrix}^T \quad (23)$$

Based on these equations, the times series  $\mathbf{A}$  of all regression coefficients can be used to perform an inverse analysis using a pseudo-inverse matrix.

$$\mathbf{A} = \Phi_{De}^\dagger \mathbf{Z}'_{De} \quad (24)$$

### 3.5. ISSUE-5: uncertainty propagation and sensitivity analysis

In this study, a regression equation for a linear combination is used for the ROM model, as shown in Equation (14). This equation allows us to determine the propagation of uncertainty from the expected value characteristics analytically. The matrix, containing only the regression coefficients corresponding to the input parameter COMPl in Equation (19), is defined as  $\mathbf{A}_l^{comp} \in \mathbb{R}^{r_m \times m}$ .

$$\mathbf{A}_l^{comp} = \begin{bmatrix} \mathbf{a}_1^{(l)} & \mathbf{a}_2^{(l)} & \cdots & \mathbf{a}_{r_m}^{(l)} \end{bmatrix}^T \quad (25)$$

Using the POD spatial mode  $\tilde{\Phi} \in \mathbb{R}^{n \times r_m}$ , this matrix is transformed into the node-element-influencing value  $\alpha_l \in \mathbb{R}^{n \times m}$  as

$$\alpha_l = \tilde{\Phi} \mathbf{A}_l^{comp} \quad (26)$$

The above equations indicate that matrix  $\mathbf{V}^{est} \in \mathbb{R}^{n \times m}$ , comprising the estimated variance of the FEM nodal displacements and the estimated variance of the elemental stresses (propagated by the uncertainties in the input parameter settings), can be calculated from the expected value characteristics by performing an operation on each sequence element as shown below.

$$\mathbf{V}^{est} = \sum_{l=1}^{r_c} \lambda_l^{z_p} \alpha_l^{\odot 2} \quad (27)$$

Here,  $\lambda_l^{z_p}$  is the eigenvalue of the  $\mathbf{Z}'_p$  covariance matrix corresponding to COMPl.

We now describe how to calculate the spatial distribution of the sensitivity coefficients in the FEM calculation area. From Equation (24), we define matrix  $\mathbf{A}_0 \in \mathbb{R}^{r_m \times m}$ , from which only the constant terms are extracted.

$$\mathbf{A}_0 = \begin{bmatrix} \mathbf{a}_1^{(r_c+1)} & \mathbf{a}_2^{(r_c+1)} & \cdots & \mathbf{a}_{r_m}^{(r_c+1)} \end{bmatrix}^T \quad (28)$$

We construct matrix  $\alpha_0 \in \mathbb{R}^{n \times m}$  using the POD space

mode  $\tilde{\Phi} \in \mathbb{R}^{n \times r_m}$  in Equation (26) to transform each node or element.

$$\alpha_0 = \tilde{\Phi} \mathbf{A}_0 \quad (29)$$

Here, the performance functions are described in the following general terms:

$$\mathbf{g} = \mathbf{R} - \mathbf{S} \quad (30)$$

For instance, when we focus on the  $y$ -direction displacement (settlement at arbitrary points),  $\mathbf{R} \in \mathbb{R}^{n_n \times m}$  is the design limiting value at arbitrary points, and it is assumed to determine the relationship with the performance of the target structure in advance. Here,  $\mathbf{R}$  is assumed to be a normal distribution with a variance of  $\sigma_{\mathbf{R}}^2$ , and it is assumed to be a constant value throughout the calculation region.  $\mathbf{S} \in \mathbb{R}^{n_n \times m}$  denotes the numerical analysis results (i.e. the calculated physical parameter spatial distribution time series).  $n_n$  denotes the number of total nodes; however,  $n_n$  replaces  $n_e$  (the number of total elements) in cases wherein the excess water pressure ratio is investigated.

$$\mathbf{S} = \alpha_0^{dy} + \sum_{l=1}^{r_c} \tilde{y}^{(l)} \alpha_l^{dy} \quad (31)$$

where  $\alpha_0^{dy} \in \mathbb{R}^{n_n \times m}$  and  $\alpha_l^{dy} \in \mathbb{R}^{n_n \times m}$  are the portion matrix of matrices  $\alpha_0$  and  $\alpha_l$ , respectively; they correspond to the target physical quantity (e.g.  $y$ -direction displacement).  $\tilde{y}^{(l)}$  is the principal component score corresponding to COMPl.

The following equations denote the vectors representing the time-series changes in the mean and variance of  $\mathbf{S} \in \mathbb{R}^{n_n \times m}$ .

$$\mu_{\mathbf{S}} = \alpha_0^{dy} \quad (32)$$

$$\sigma_{\mathbf{S}}^2 = \sum_{l=1}^{r_c} \lambda_l^{(z_p)} (\alpha_l^{dy})^{\odot 2} \quad (33)$$

From Equation (33), the spatial distribution time series of the sensitivity coefficients of COMPl,  $\mathbf{c}_l^2 \in \mathbb{R}^{n_n \times m}$ , can be calculated as:

$$\mathbf{c}_l^2 = \{\lambda_l^{(z_p)} (\alpha_l^{dy})^{\odot 2}\} \oslash (\sigma_{\mathbf{R}}^2 + \sigma_{\mathbf{S}}^2) \quad (34)$$

## 4. Application to a simple example

### 4.1. Problem outline

Figure 2(a) shows an FEM model of a sample soil section ( $n_n = 464$  and  $n_n = 424$ ). This model is used as the example shown in the LIQCA summaries (Liquefaction analysis method LIQCA Development group, 2007). It was created for dynamic centrifugal model

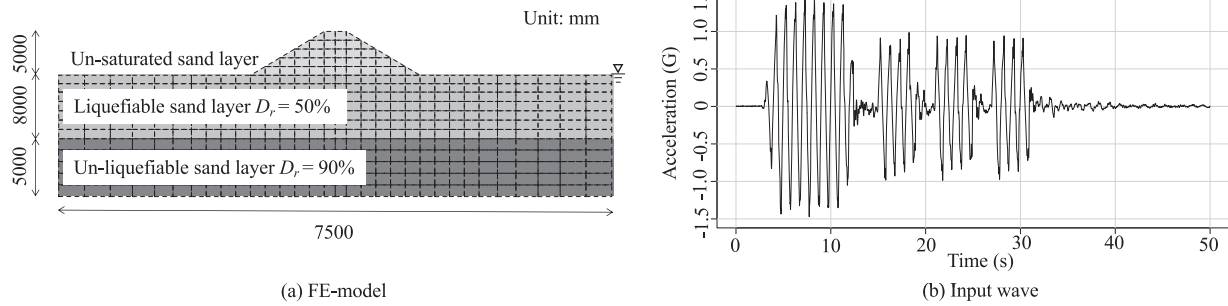


**Figure 2.** Numerical analysis model and input wave ((a) FE-model (b) Input wave).

tests (50 G) (Matsuo, Okamura, and Tamoto, 2000) at the Public Works Research Institute, Japan. The dimensions of the figure were converted to the scale of an actual structure using scaling laws. The topmost soil layer is an embankment, which is followed by a liquefiable sand layer (both of which comprise Edosaki sand set to approximately  $D_r = 50\%$  immediately below the embankment) and an unliquefiable sand layer (consolidated No.7 silica sand ( $D_r = 90\%$ )). Moreover, both boundaries of the experiment soil vessel were set as rigid walls, which do not undergo shear deformation. To meet the experimental requirements, the sides of the FEM model were set with horizontally fixed and vertically free boundary conditions and with a bottom-fixed undrained boundary condition. Plane strain elements were used, and for all elements the cyclic elastoplastic model of sand (Oka et al., 1999) was adopted.

The cyclic elastoplastic model is developed, especially for simulating the liquefaction, based on a generalised nonassociated flow rule using nonlinear kinematic hardening rule. In this model, the overconsolidation boundary surface to control dilatancy, plastic strain dependency of the shear stiffness, and fading memory of the initial anisotropy are considered.

Figure 2(b) shows the time series of the input ground motion. A principal shock of 1.5 G (approximately 5 s) and three later-phase waves of 1.0 G were used as the rigid foundation inputs. The embankment and liquefiable sand layer were provided the same input parameters; the previously mentioned DE (Table 2) was followed to modify the input parameters and conduct the analysis. In all cases, the unliquefiable layer used the deterministic values of DS-2 (unliquefiable sand layer; No.7 silica soil; and  $D_r = 90\%$ ) as its input parameters.

The top seven input parameters in Table 2 (the initial void ratio  $e_0$ , compression index  $\lambda$ , swelling index  $\kappa$ , overconsolidation ratio  $OCR^*$ , nondimensional initial shear stiffness  $G_0/\sigma'_m$ , stress ratio at failure  $M_f^*$ , and stress ratio at phase transformation  $M_m^*$ ) can be determined via experiments, such as consolidation test and

triaxial test. The remaining seven parameters (nonlinear hardening parameters  $B_0^*$ ,  $B_1^*$ ,  $\gamma_p^*$ , and  $\gamma_e^*$ ; and dilatancy parameters  $D_0^*$  and  $n$ ) are determined by curve fitting in comparison with the experimental results, such as liquefaction resistance curve, stress–strain relationship, effective stress path of the cyclic triaxial test, and the relationship between shear stiffness and shear strain obtained from the dynamic deformation test.

The limit state of the calculation was set to verify that the ‘settlement amount at the top end of the embankment (i.e.  $y$ -direction displacement) does not exceed half of the embankment height  $H(H/2)$ ’; a series of analyses were conducted until the reliability evaluation. Notably, for calculating the spatial distribution of the sensitivity coefficient, it is necessary to define the limit state at an arbitrary point on the target structure. Although it is not practical, the same limitations are applied at all points in this case.

#### 4.2. Principal component analysis (PCA) of the input parameters

The biplots of the principal component scores of the input parameters, COMP1 and COMP2, are shown in Figures 3(a) and 3(b), respectively; the contributions of each COMP are shown in Figure 3(c).

Although Figures 3(a) and (b) are same; in (b), the number DS-I, listed in Table 1, and the descriptions of the characteristics of each quadrant are provided. The third and fourth quadrants are dominated by loose laboratory sand. In the first and second quadrants, samples obtained from the field are distributed, showing mostly artificial reclaimed soil in the first quadrant and naturally deposited ground in the second quadrant.

The soil features could be classified in these biplots. The contribution rates from COMP1 to COMP3 exceeded 60% of the amount of input information. The black square points in Figure 3(a) denote the 19 parameter sets collected from the data bank, and the mode value (i.e. principal component factor) of each

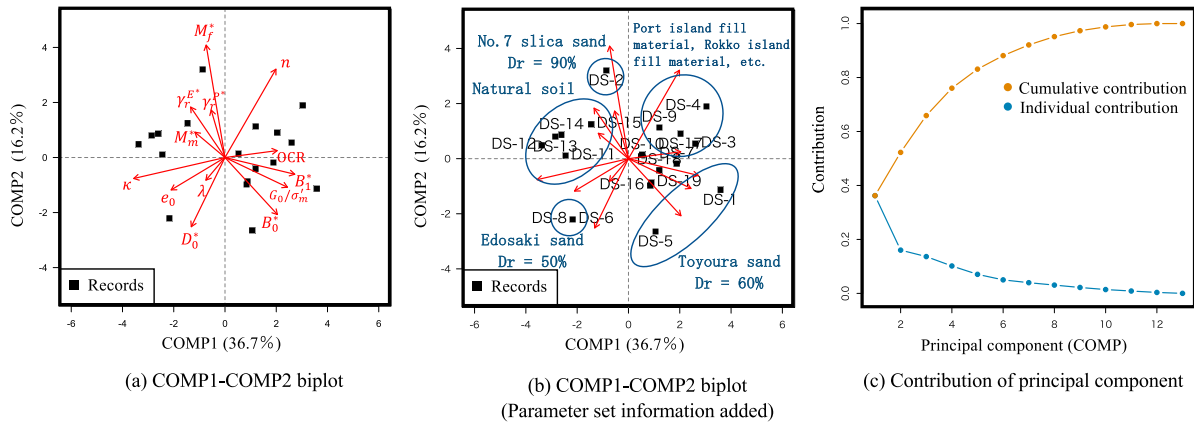


**Figure 3.** Principal component analysis (PCA) results of the input parameters ((a) Comp1-Comp2 biplot, (b) Comp1-Comp2 biplot with input parameter set information, (c) Contribution of principal component).

parameter is denoted by an arrow. Although the physical meanings of the principal component space of the input parameters are not considered in this paper owing to technical limitations, the interpreted physical meaning of each principal component is summarised as follows:

- COMP1: Comprehensive index of rigidity
- COMP2: Comprehensive index of dilatancy
- COMP3: Comprehensive index of persistence after reaching the phase transformation line

Thus, we conducted analysis with dimension number  $r_c = 3$ , where COMP1 and COMP2, which have engineering-based definitions, and COMP3 (total contribution rate of 65%) are used. It is possible to impart objectivity using statistical modelling (e.g. sparse modelling (Tibshirani, 1996)); however, this study is a proposal for a reliability analysis scheme, and therefore, we limit ourselves to a simple analysis. The above-mentioned decisions were made only for convenience. Notably, the input parameter set may not be well contracted (i.e. sparse space has not been found) by applying simple linear mode decomposition (PCA). In future, we plan to apply and compare nonlinear mode decomposition methods (e.g. K-SVD (Aharon, Elad, and Bruckstein, 2006; Otake, Kodama, and Watanabe, 2019b), kernel PCA (Schölkopf, Smola, and Müller, 1998), robust PCA (Candès et al., 2011), the introduction of multiresolution representation, etc.) to investigate more appropriate contractions with feature extraction. Further, it is critical to expand the data, check the prediction performance, and generalise the performance based on cross-validation methods and information criteria.

#### 4.3. Mode decomposition (POD) for numerical analysis

The contribution rates of the POD spatial modes are shown in Figure 4. The contribution of POD spatial mode 1 is extremely high; 98% of the amount of information is provided by POD spatial mode 3. The POD spatial modes 1–5 are plotted in the ascending order of eigenvalues, as shown in Figure 5. The deformation (i.e. horizontal and vertical displacements) modes are shown as nodal displacements, with the excess pore water pressure ratio modes shown with element colour. Figure 6 shows the relationship between the time series component coefficient of POD spatial modes 1–3 and the input waveform.

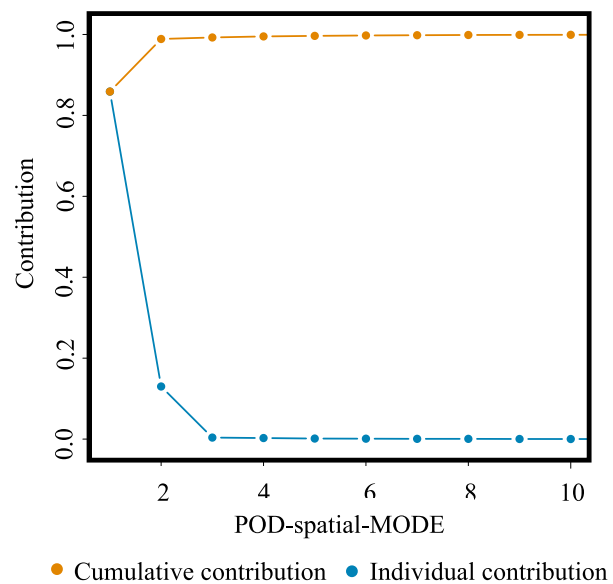


**Figure 4.** Contribution rate of each POD spatial mode calculated from the numerical analysis results.

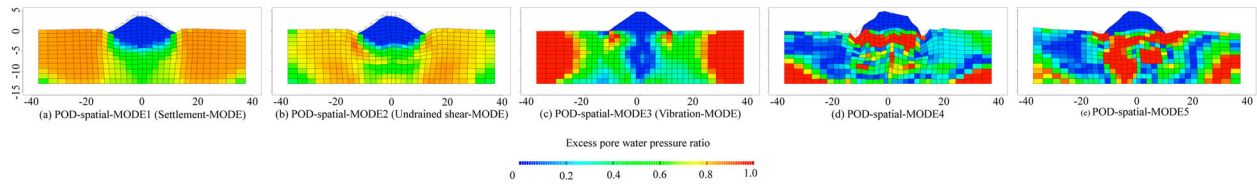


Figure 5. POD spatial modes  $\{u_1, u_2, u_3, u_4, u_5\}$ .

As shown in Figure 5(a), the embankment in POD spatial mode 1 shows settling tendencies and has high excess pore water pressure tendencies in all parts, except in those immediately below the embankment body, where the confining pressure is high. Figure 6 shows that the time series component coefficient controls the embankment behaviour after 12 s, which is when the first wave ends (i.e. when most of the foundation ground has liquefied). This can be interpreted as a fundamental settlement mode, governing the target structure, that accompanies the embankment foundation ground liquefaction, and henceforth, it is referred to as ‘Settlement-MODE’.

As seen in Figure 5(b), POD spatial mode 2 shows settling tendencies similar to those of POD spatial mode 1; however, the excess pore water pressure ratio behaviour is different. The excess pore water pressure ratio is particularly high in the local areas at the foot of the embankment body slope. The time series component coefficient in Figure 6 indicates large contributions to the embankment behaviour during the 12 s from the start of the vibrations to the end of the first wave (when most of the foundation ground has liquefied). However, its subsequent contributions become small. We refer to this as the ‘Undrained shear-MODE’, where shearing is repeated under undrained conditions.

As seen in Figures 5(a)–(c), POD spatial mode 3 is different from POD spatial modes 1 and 2, and this mode does not contribute to the residual displacement of the embankment body. The lower foot of the slope and fixed side boundary areas have high excess pore

water pressure ratios, which is referred to as the ‘Vibration-MODE’.

As shown in Figure 4, the physical meanings of the POD spatial modes, 4 and 5, are difficult to interpret in an engineering sense. Therefore, we construct an alternative model using POD spatial modes 1–3, and the number of dimensions (i.e. horizontal displacement  $n_n$  dimensions, vertical displacement  $n_n$  dimensions, and excess pore water pressure ratio  $n_e$  dimensions) was found to decrease significantly from  $2n_n + n_e = 1352$  to 3.

#### 4.4. Bayesian inference results (input parameter update results)

The Bayesian inference results, derived using a portion of the DS-1 information from the initial data listed in Table 1, are shown in Figure 7. Three patterns of the Bayesian inference results are shown in Figure 7(a) (left: update by  $e_0$ , middle: update by  $e_0$  and  $G_0/\sigma'_m$ , and right: update by  $e_0$ ,  $G_0/\sigma'_m$  and  $M_f^*$ ). The observed errors in the Bayesian inference are assumed to be 10%. As mentioned earlier, Bayesian updating is performed analytically in the proposed framework. Here, we generate random numbers using the to prior and posterior distributions and overlap them to visualise the effect of this Bayesian update. In Figure 7(a), parameter sets created from prior distributions (PRIOR: 10,000 generates) are shown in light grey and those created from the posterior distributions following Bayesian inference (POST: 10,000 generates) are shown in dark grey. Figure 7(b) shows the estimated range of the parameter set of the posterior distribution (POST) corresponding to three update cases (left: update by  $e_0$ , middle: update by  $e_0$  and  $G_0/\sigma'_m$ , and right: update by  $e_0$ ,  $G_0/\sigma'_m$  and  $M_f^*$ ). The range from the average value  $\pm 1\sigma$  (i.e. one standard deviation) was standardised and plotted in grey for relative comparisons.

The parameter set in DS-1, set up by experts, is shown in red. The left side of the figures indicates that there were no major differences between the prior and posterior distributions. This implies that the  $e_0$  information does not contribute significantly to parameter

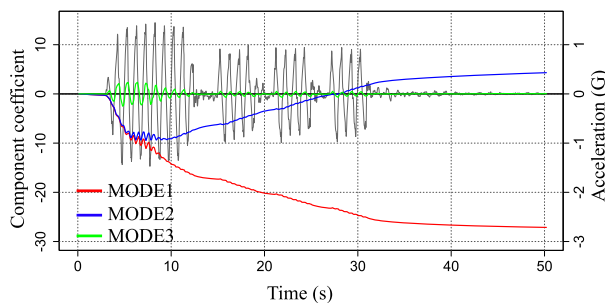
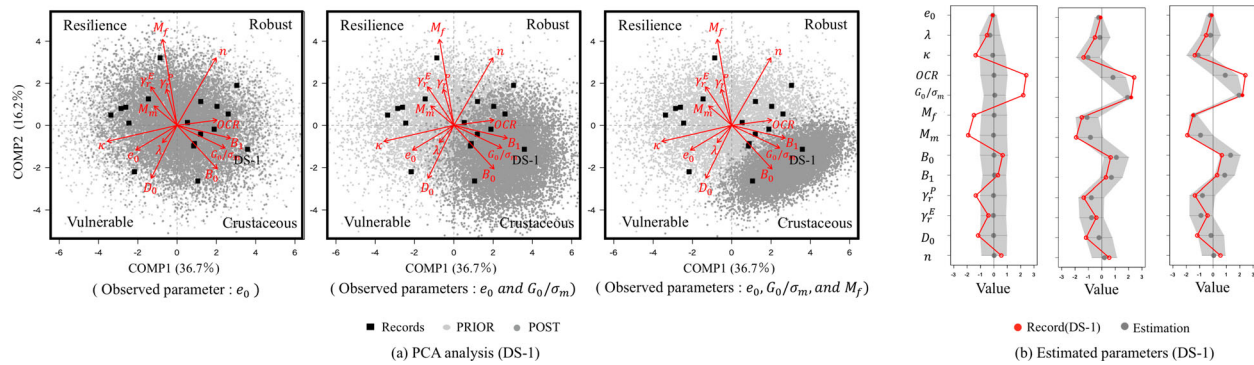


Figure 6. POD spatial mode coefficients time series.





**Figure 7.** Parameter update results (DS-1) ((a) Bayesian inference results in the biplot figure, (b) Estimated parameter distribution).

estimation in DS-1. In contrast, the middle ( $G_0/\sigma'_m$  information added) and right ( $G_0/\sigma'_m$  and  $M_f^*$  information) rows of the figure indicated that there are large differences between the prior and posterior distributions; further, posterior distributions are closer to the parameter sets, set up by experts.

A detailed account of this is beyond the technical scope of this paper. However, we do confirm update sensitivity based on a few physical parameters that can be observed in the field. In the future, we plan to expand the study to collect sets of input parameters and verify their validity based on objective analysis, such as by using the cross-validation method.

#### 4.5. Calculated results of ROM

##### 4.5.1. ROM simulation (estimate of the expectation)

The DEs near the average of the prior distribution, principal component scores, and input parameter sets of COMP1-3 are listed in Table 2. A numerical analysis was conducted with the five DEs shown here to create an alternative model (ROM). The FEM analysis results obtained using the input parameter sets corresponding to the average values of the prior distribution are shown in Figure 8(a). The spatial distribution snapshots of the deformation plots and excess pore water pressure ratio (displayed by a colour gradient in the element) are shown at time points 5 s, 7.5 s, 10 s, 20 s, 30 s, and 40 s. The ROM simulation results under the same conditions as those shown in Figure 8(a) are depicted in Figure 8(b). Both the FEM analysis and ROM simulations qualitatively correspond with each other at each time point. The results where a time series correction factor was applied to each POD spatial mode are shown in Figures 8(c) and (d). Figure 8(b) was obtained from the combination of these three POD spatial modes.

Figure 9(a) focuses on the deformation of the top end of the embankment body (red) and the excess pore

water pressure ratio (blue), immediately below the embankment body, in the average value case of the prior distribution (i.e. DE-1). The figure compares the time series behaviour of the FEM analysis and the ROM simulation. From left to right, Figure 9(a) shows the positions in the embankment where the structural displacements and time series are compared, time series of the foundation input waveform, time series of the excess pore water pressure ratio immediately below the embankment, time series of the horizontal displacement ( $x$ -displacement) of the top end of the embankment body, and time series of the vertical displacement ( $y$ -displacement) of the top end of the embankment body.

The FEM analysis results are represented by a solid line, and the ROM simulation results are shown with a dotted line. The results confirm that the ROM accurately simulated the FEM analysis results at each time point. Figure 9(b) shows the same comparisons for DE-2. Some minor deviations are observed between the FEM analysis and ROM simulations results in the time series of the excess pore water pressure ratio. Overall, the ROM simulations accurately characterises the features of the time series behaviour.

##### 4.5.2. Uncertainty propagation and sensitivity analysis

Figure 10(a) shows the results of the ROM simulation for the average value of the prior distribution (DE-1) and the uncertainty propagation analysis. The results of the uncertainty analysis results are shown as the range of  $\pm 1\sigma$  (hatched areas) of the ROM analyses (grey hatching).

From left to right, Figure 10(a) shows the embankment structure, time series of excess pore water pressure ratio just below the embankment, time series of horizontal displacement of the top of the embankment ( $x$ -direction), time series of vertical displacement of the top of the embankment ( $y$ -direction), and failure



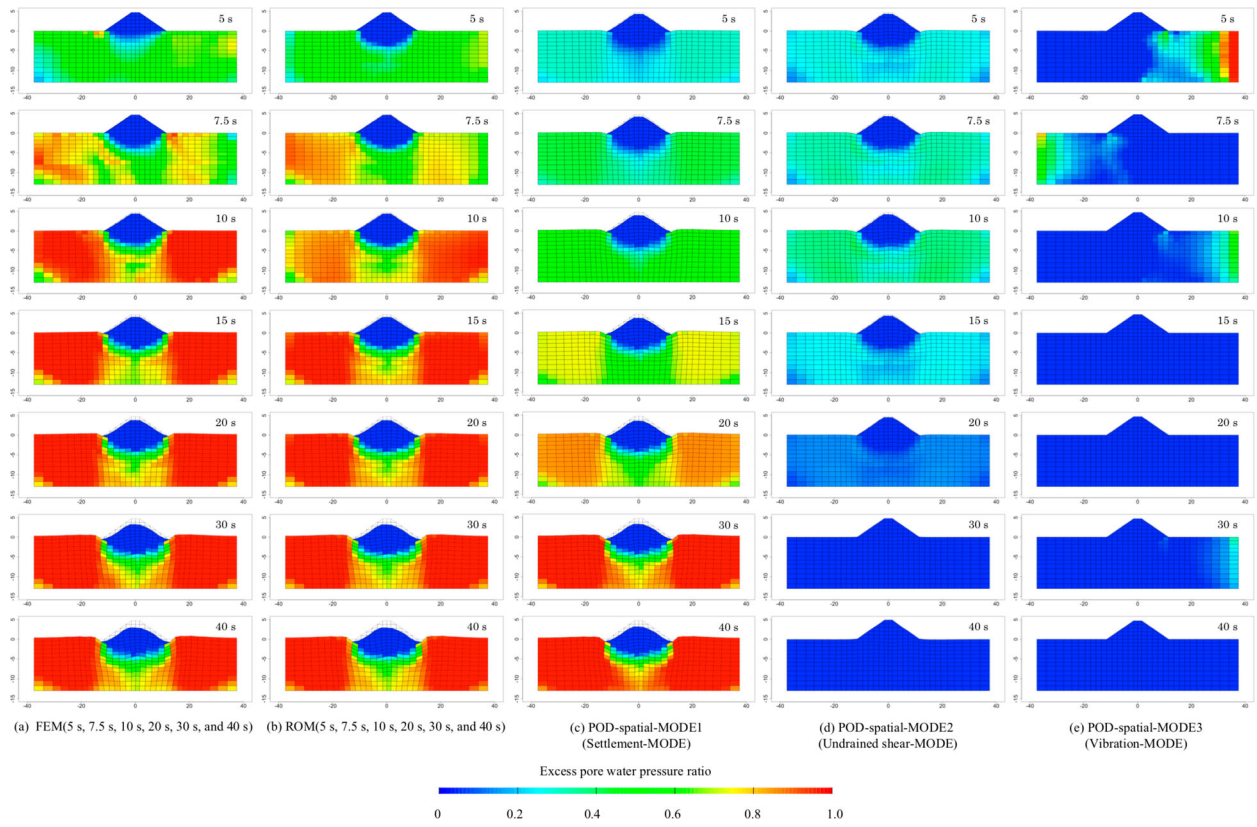


**Figure 8.** FEM and ROM comparisons for each POD mode (5 s, 7.5 s, 10 s, 20 s, 30 s, and 40 s) ((a) FEM analysis, (b) ROM, (c) POD-spatial-MODE1, (d) POD-spatial-MODE2, and (e) POD-spatial-MODE3).

probability with one-half of the embankment height as the settlement limit.

At an arbitrary time point, the failure probability was determined by setting the displacement limit values as random variables and analytically calculation using the expected value characteristics (as employed in FOSM and FORM). The failure probability between the second and

third later-phase waves increased dramatically and reached approximately  $10^{-1}$  at the end of the analysis (50 s).

Similar to Figure 10(a), Figure 10(b) shows the results of the ROM and uncertainty propagation analyses corresponding to the posterior distribution based on a portion of the information in DS-1 ( $e_0$ ,  $G_0/\sigma'_m$ ,  $M_f^*$ ).

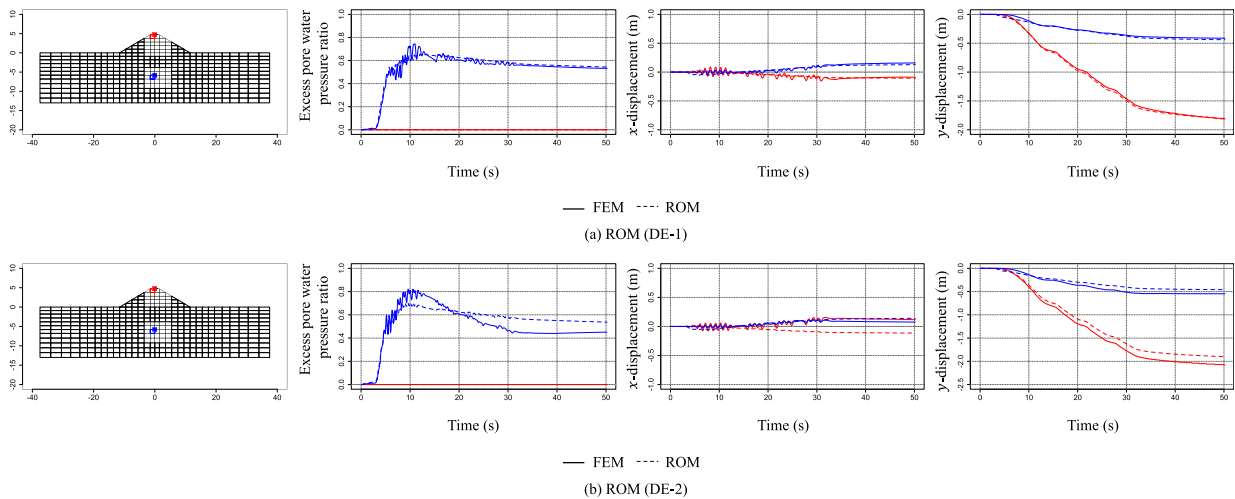


**Figure 9.** Calculated ROM results ((a) DE-1 and (b) DE-2).

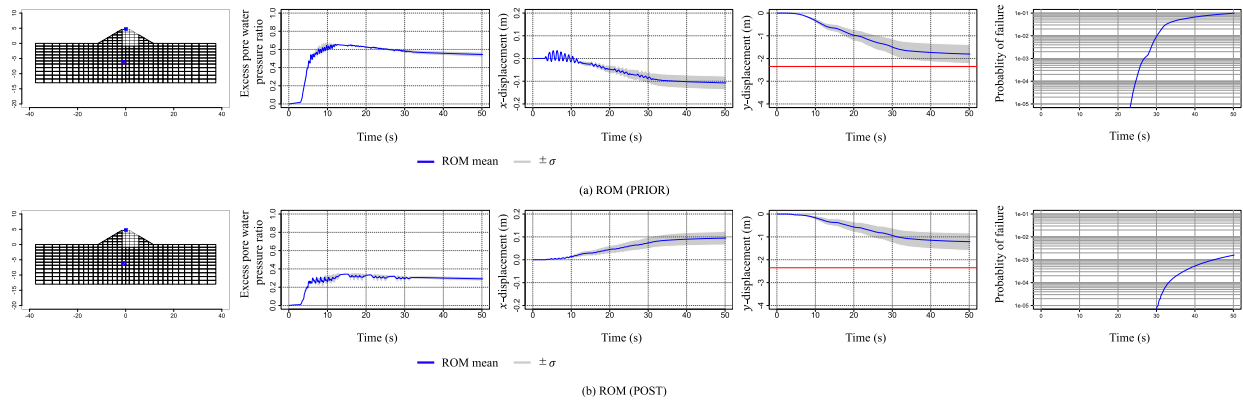


**Figure 10.** Updated ROM results ((a) PRIOR and (b) POSTERIOR).

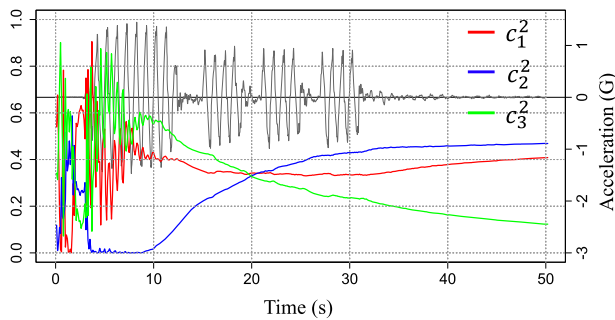


**Figure 11.** Sensitivity coefficient time series at the top of the embankment ( $c_1^2$ ,  $c_2^2$ , and  $c_3^2$ ), COMP1: Comprehensive index of rigidity, COMP2: Comprehensive index of dilatancy, COMP3: Comprehensive index of persistence after reaching the phase transformation line.

The magnitude and trend of the time series of the failure probability vary considerably, depending on the input parameters, leading to different decisions in the two cases. Figure 11 shows the sensitivity coefficient time series for COMP1, COMP2, and COMP3 at the top of the embankment. COMP1 is interpreted as the ‘Comprehensive index of rigidity’, and it makes a significant contribution to the overall analysis time. COMP2 is interpreted as the ‘Comprehensive index of dilatancy’ after the main shaking, and its contribution gradually increases after the soil foundation liquefies. COMP3 is interpreted as the ‘Comprehensive index of stickiness after reaching the phase transformation line’, and it tends to exhibit a significant contribution during the main dynamics and gradually decreases as

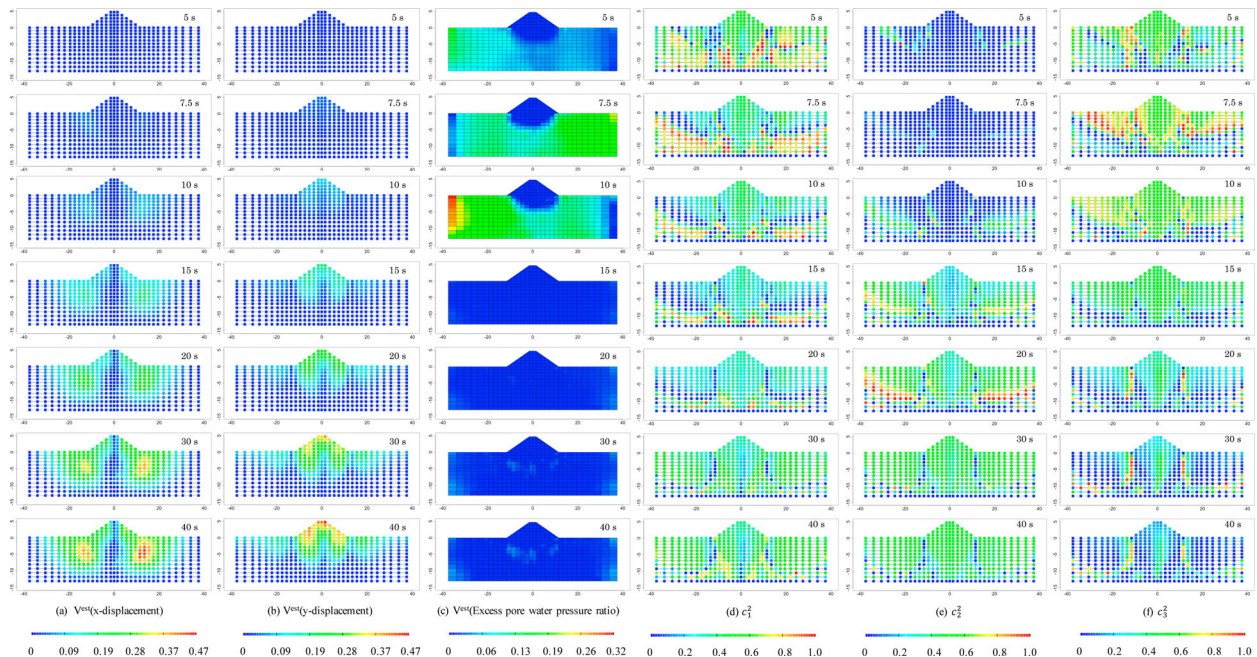


**Figure 12.** Spatial distributions of the variance and sensitivity coefficients ( $V_{est}$ ,  $c_1^2$ :COMP1,  $c_2^2$ :COMP2, and  $c_3^2$ :COMP3).

the contribution of COMP2 increases. Thus, the time series of the sensitivity coefficients were found to be related to the physical meaning of each COMP.

Figure 12 shows the spatial distribution time series for the variance and sensitivity coefficients (5 s, 7.5 s, 10 s, 20 s, 30 s, and 40 s). From left to right, Figure 12 shows the spatial distribution of the horizontal displacement ( $x$ -displacement), vertical displacement ( $y$ -displacement), excess pore water pressure ratio, and sensitivity coefficient of  $c_1^2$ :COMP1,  $c_2^2$ :COMP2, and  $c_3^2$ :COMP3. The variance of the calculated engineering indices (i.e. displacement and stress) and the sensitivity coefficients corresponding to each COMP are calculated as spatio-temporal information. Thus, we can observe the spatial characteristics of each calculated parameter at arbitrary time, as shown in this figure. Using this information, the difficulty in predicting the physical behaviour of a facility from engineering viewpoints can be analysed. Further, it is considered to provide critical information for decision making while exploring locations for additional soil investigations or monitoring.

## 5. Conclusions

In this paper, we proposed a simplified reliability analysis method that preserves the spatiotemporal characteristics of earth structures to develop a practical method for controlling the failure mode under accidental loading. The main conclusions are listed below.

- (1) An ROM model was proposed that independently performs modal decomposition of the input parameters and numerically analyses the time series data. This model combines these two aspects using simple linear regression analysis.
- (2) The input parameters for numerical analysis could be effectively determined by Bayesian updating from the partial parameters observed in the field.
- (3) The proposed methods were applied to the analysis of seismic deformation of embankments on liquefied ground, and an actual procedure was presented.
- (4) The results showed that reliability analysis could be performed without losing the spatiotemporal information (information about the failure modes) obtained from the numerical analysis.
- (5) The proposed method follows the concept of FORM, which is a traditional reliability analysis method. The variance and sensitivity coefficients of the input parameters were analytically computed over the entire numerical analysis space. This information is suggested to be essential for facility managers to take decisions related to the requirement for additional investigations.

In this study, we focused on the presentation of the framework and issues related to individual element techniques that need to be investigated. The mode decomposition (POD and PCA), which plays a central role in the proposed framework, is an eigenvalue problem with a linear base. Further, issues related to the application of this method to nonlinear problems need to be resolved. We intend to expand this work to include nonlinear mode decompositions in the future. In addition, we intend to analyse the effectiveness of the proposed method, by conducting geotechnical observations of the PCA results of the input parameters, and the validity of the proposed method using FEM-based Monte-Carlo simulations.

Finally, we compared our results with those of the direct reliability analysis. The example used in this study focused on the time series of the deformation of the top end of the embankment. In future, we intend to incorporate case studies that estimate the failure modes of target structures by focusing on the temporal changes over the entire spatial domain, and on multiple points and parameters to develop control methods for brittle failure modes (i.e. contributions from robustness and resilience).

## Disclosure statement

This study was supported by JSPS KAKENHI Grand-in-Aid (20H00264).

## ORCID

Yu Otake  <http://orcid.org/0000-0002-4879-540X>

Shogo Muramatsu  <http://orcid.org/0000-0002-2990-1238>

## References

- Aharon, M., M. Elad, and A. Bruckstein. 2006. “\$rm K\$-svd: An Algorithm for Designing Overcomplete Dictionaries for Sparse Representation.” *IEEE Transactions on Signal Processing* 54: 4311–4322.
- American Association of State Highway and Transportation Officials. 2003. *Guide Manual for Condition Evaluation and Load and Resistance Factor Rating (LRFR) of Highway Bridges*. Washington, DC.
- American Association of State Highway and Transportation Officials. 2004. *AASHTO LRFD Bridge Design Specifications*. 3 ed. Washington, DC.
- Berkooz, G., P. Holmes, and J. Lumley. 2003. “The Proper Orthogonal Decomposition in the Analysis of Turbulent Flows.” *Annual Review of Fluid Mechanics* 25: 539–575.
- Bruneau, M., S. Chang, R. Eguchi, G. Lee, T. O’Rourke, A. Reinhorn, M. Shinozuka, K. Tierney, W. Wallace, and D. Winterfeldt. 2003. “A Framework to Quantitatively Assess and Enhance the Seismic Resilience of Communities.” *Earthquake Spectra -- EARTHQ SPECTRA* 19: 733–752.
- Candès, E. J., X. Li, Y. Ma, and J. Wright. 2011. “Robust Principal Component Analysis?” *J. ACM* 58 (3): 1–39.



- CEN, EN 1997-1 Eurocode 7. 2004. *Geotechnical Design – Part 1: General Rules*.
- Chatterjee, A. 2000. “An Introduction to the Proper Orthogonal Decomposition.” *Current Science* 78 (7): 808–817.
- Ching, J., and K.-K. Phoon. 2019. “Constructing Site-specific Multivariate Probability Distribution Model Using Bayesian Machine Learning.” *Journal of Engineering Mechanics* 145: 04018126.
- Ching, J., and K.-K. Phoon. 2020. “Constructing a Site-specific Multivariate Probability Distribution Using Sparse, Incomplete, and Spatially Variable (music-x) Data.” *Journal of Engineering Mechanics* 146: 04020061.
- Cornell, C. A. 1969. “A Probability-based Structural Code.” *ACI Journal Proceedings* 66 (12): 974–985.
- Danjo, W., M. Mimura, Y. Higo, N. Kitada, T. Hamada, and R. Tanaka. 2018. “Research Based on Brittleness Evaluation During Earthquakes Based on Geoinformatics Databases – Case Study of West Hirano, Osaka.” In *53rd Geotechnical Engineering Research Conference*, 253–254. in Japanese.
- Hasofer, A. M., and N. C. Lind. 1974. “Exact and Invariant Second Moment Code Format.” *Journal of the Engineering Mechanics Division, ASCE* 100: 111–121.
- Hirota, N., T. Takeuchi, Y. Higo, and T. Kiriya. 2017. “Basic Research Relating to MPM Accuracy Evaluations Based on Liquefaction Analysis.” In *52nd Geotechnical Engineering Research Conference*, 1581–1582. in Japanese.
- Honda, R., M. Akiyama, S. Kataoka, Y. Takahashi, A. Nozu, and Y. Muro. 2016. “Seismic Design Method to Consider “anti-catastrophe” Concept – a Study for the Draft of Design –.” *Journal of Japan Society of Civil Engineers, Ser. A1 (Structural Engineering & Earthquake Engineering (SE/EE))* 72 (4): I\_459–I\_472.
- Hoshiya, M., and I. Yoshida. 1996. “Identification of Conditional Stochastic Gaussian Field.” *Journal of Engineering Mechanics* 122 (2): 101–108.
- ISO2394. 1998. *General Principles on Reliability for Structures*.
- ISO2394. 2015. *General Principles on Reliability for Structures*.
- Japan Port and Harbor Association (JPHA). 2007. *Technical Standards and Commentaries for Port and Harbor Facilities in Japan*.
- Japan Port and Harbor Association (JPHA). 2018. *Technical Standards and Commentaries for Port and Harbor Facilities in Japan*.
- Japan Road Association (JRA). 1996. *Specifications for Highway Bridges and Commentary*, Lower structure edition.
- Japan Road Association (JRA). 2017. *Specifications for Highway Bridges and Commentary*, Lower structure edition.
- Jolliffe, I. T. 2002. *Principal Component Analysis*. 2nd ed. Springer Series in Statistics. New York: Springer-Verlag.
- Jongejan, R., B. Maaskant, W. Horst, F. Havinga, N. Roode, and H. Stefess. 2013. “The vnk2 Project: A Fully Probabilistic Risk Analysis for the Major Levee Systems in the Netherlands.” In *5th International Conference on Flood Management (ICFM5)*.
- Liang, Y., H. Lee, S. Lim, W. Lin, K. Lee, and C. Wu. 2002. “Proper Orthogonal Decomposition and Its Applications – Part I: Theory.” *Journal of Sound and Vibration* 252: 527–544.
- Liquefaction analysis method LIQCA Development group. 2007. *LIQCA2D07*, 2007 published edition.
- Matsuo, O., M. Okamura, and S. Tamoto. 2000. “Report on Dynamic Centrifuge Model Tests relating to Seismic Countermeasure Effects on Solidification Treatment of the Toe of Embankment.” *Report No. 3688*, Public Works Research Institute.
- Oka, F., A. Yashima, T. Shibata, M. Kato, and R. Uzuoka. 1994. “FEM-FDM Coupled Liquefaction Analysis of Porous Soil Using An Elasto-plastic Model.” *Applied Scientific Research* 52: 209–245.
- Oka, F., A. Yashima, A. Tateishi, Y. Taguchi, and A. Yamashita. 1999. “A Cyclic Elasto-plastic Constitutive Model for Sand Considering a Plastic-strain Dependence of the Shear Modulus.” *Géotechnique* 49 (5): 661–680.
- Otake, Y., and Y. Honjo. 2012. “Reliability based design on long irrigation channel considering the soil investigation locations.” *GeoCongress 2012 : State of the Art and Practice in Geotechnical Engineering*, 2836–2845 (03).
- Otake, Y., S. Kodama, and S. Watanabe. 2019b. “Improvement in the Information-oriented Construction of Temporary Soil-retaining Walls Using Sparse Modeling.” *Underground Space* 4 (3): 210–224.
- Otake, Y., S. Watanabe, Y. Higo, and K. Shigeno. 2019a. “Validation of Numerical Analysis based on Mode Decomposition.” In *Proc. 7th International Symposium on Geotechnical Safety and Risk (ISGSR 2019)*, 679–684.
- Otake, Y., S. Watanabe, and T. Mizutani. 2021. “Improvement of Side Resistance Prediction for Pile Foundation Using Construction Information.” *Canadian Geotechnical Journal* 58 (4): 496–513.
- Pearson, K. 1901. “On Lines and Planes of Closest Fit to Systems of Points in Space.” *The London, Edinburgh, and Dublin Philosophical Magazine and Journal of Science* 2 (11): 559–572.
- Railway Technical Research Institute (RTRI). 2013. *Design Standards for Railway Structures and Commentary*, Soil structure edition.
- Rezaei, S., and A. Der Kiureghian. 2010. “Simulation of Synthetic Ground Motions for Specified Earthquake and Site Characteristics.” *Earthquake Engineering & Structural Dynamics* 39: 1155–1180.
- Schölkopf, B., A. Smola, and K.-R. Müller. 1998. “Nonlinear Component Analysis As a Kernel Eigenvalue Problem.” *Neural Computation* 10 (5): 1299–1319.
- Schultz van Haegen, M. 2016. *Fundamentals of Flood Protection*. Delft, the Netherlands: Minister of Infrastructure and the Environment.
- Schweckendiek, T. 2014. “On Reducing Piping Uncertainties – A Bayesian Decision Approach.” Ph.D. thesis.
- Sirovich, L. 1987. “Turbulence and the Dynamics of Coherent Structures. I -- Coherent Structures. Ii -- Symmetries and Transformations. Iii -- Dynamics and Scaling.” *Quarterly of Applied Mathematics* 45: 561–590.
- Tibshirani, R. 1996. “Regression Shrinkage and Selection Via the Lasso.” *Journal of the Royal Statistical Society* 1 (Series 58): 267–288.
- Yoshida, I., Y. Tasaki, Y. Otake, and W. Stephen. 2018. “Optimal Sampling Placement in a Gaussian Random Field Based on Value of Information.” *ASCE-ASME Journal of Risk and Uncertainty in Engineering Systems, Part A: Civil Engineering* 4 (2): 04018018: 1–11.
- Zienkiewicz, O. C., and T. Shiomi. 1984. “Dynamic Behaviour of Saturated Porous Media; the Generalized Biot Formulation and Its Numerical Solution.” *International Journal for Numerical and Analytical Methods in Geomechanics* 8 (1): 71–96.